Optical and Quantum Electronics **26** *(1994) 1061–1078*

Theoretical analysis of a time-synchronized picosecond double-pulse branched Nd : glass laser

A. PENZKOFER, J. FURTHNER
Naturwissenschaftliche Fakultät II – Physik, Universität Regensburg, D-93040 Regensburg, Germany

Received 29 March 1993; revised 25 March; accepted 11 April 1994

The laser performance of a time-synchronized double-pulse picosecond laser system is studied theoretically by numerical simulations. The arrangement consists of an Nd : silicate glass branch, an Nd : phosphate glass branch, and a common antiresonant ring. Temporal synchronization is achieved by electrooptic *Q*-switching, acoustooptic loss modulation, and saturable absorber bleaching (mutual master–slave coupling).

1. Introduction

Time-synchronized frequency tunable ultrashort laser pulses are prerequisites for short-pulse nonlinear optical frequency mixing (sum and difference frequency generation) [1–6], short-pulse driven coherent scattering (coherent anti-Stokes Raman scattering [7, 8], coherent Stokes Raman amplification [9]) and time-resolved spectroscopic pump and probe measurements [8, 10–12].

There exist various methods for generating two time-synchronized pulses with variable frequency spacing. Nonlinear optical parametric three-photon generators, oscillators, and amplifiers convert part of the pump laser pulses to time-synchronized broadly frequency-tunable signal and idler pulses [1–3, 13]. Femtosecond laser pumped parametric oscillators are available for temporally and spectrally resolved experiments [14–16]. Picosecond [17–19] and femtosecond [20–22] light continua generated by four-photon interactions are ideal spectroscopic light sources for ultrafast spectroscopic studies. Two lasers operating at different wavelengths may be synchronized electronically [23–25]. Fixed-frequency picosecond lasers were applied to pump synchronously two dye lasers [26–31] or Ti : sapphire lasers [32, 33]. Synchronous pumping of single lasers by picosecond [34, 35] or femtosecond pump pulses [36, 37] results in two pulses of different frequency if part of the pump pulse is retained. The double-pulse operation of branched lasers was achieved by loss modulation coupling in a common mode-locking element [38, 39]. Recently two-pulse femtosecond pulse generation was achieved in two Ti : sapphire lasers with common gain medium by cross-mode-locking of the solitary pulses in the cavities [40]. In other arrangements the broad spectral fluorescence range of Ti : sapphire was fanned out to two beams in the prism-dispersed region of the femtosecond Ti : sapphire lasers and led to two-colour two-pulse operation [41, 42].

0306–8919

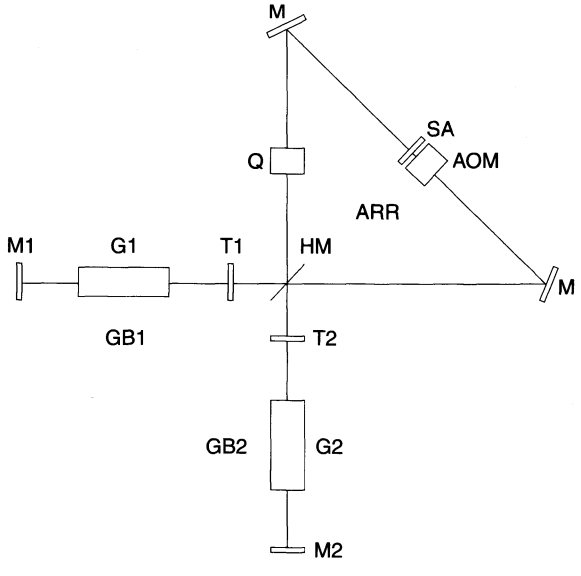

Figure 1 Arrangement of double-branch laser system: M1, M2, output mirrors; HM, 50% mirror; M, 100% mirrors; G1, G2, gain media; T1, T2, frequency tuning filters; Q, electrooptic *Q*-switch; SA, saturable absorber; AOM, acoustooptic modulator; GB1, Nd : phosphate glass gain branch; GB2, Nd : silicate glass gain branch.

In this paper we study theoretically the laser performance of a gain-branched and loss modulation combined Nd : phosphate glass–Nd : silicate glass double laser system [39] having a common electrooptic *Q*-switch [39, 43, 44] (simultaneous start of laser action in both branches), acoustooptic modulator [45, 46] (active mode-locking), and saturable absorber [47] (passive mode-locking). Experimental results of this system have been presented in [39]. First the performance of the separately operated Nd : phosphate glass laser and the Nd : silicate glass laser is analysed. Then the combined laser operation is investigated.

2. Laser model

The modelled laser system is shown in Fig. 1. It consists of two gain branches and a loss part that is incorporated in an antiresonant ring structure [48]. The gain branch GB1 includes the

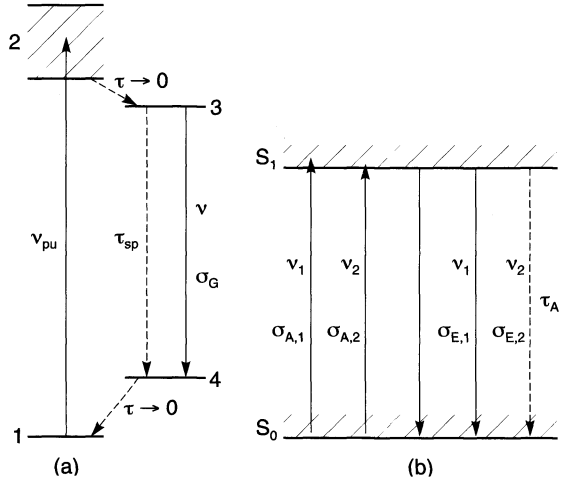

Figure 2 (a) Energy level scheme of gain medium. (b) Energy level scheme of saturable absorber medium.

Nd : phosphate glass gain medium G1 and the birefringent frequency tuning filter T1 [49]. The gain branch GB2 is built up of the Nd : silicate glass gain medium G2 and the birefringent filter T2. In the antiresonant ring ARR an electrooptic Q-switch Q [43, 44], a saturable absorber SA [47], and an acoustooptic modulator AOM [45, 46] are incorporated.

The dynamics of the gain medium is described by a four-level system with fast relaxation of excited ions from the pump band 2 to the upper laser level 3 ($\tau \rightarrow 0$) and fast relaxation of ions in the lower laser level 4 back to the ground state 1 ($\tau \rightarrow 0$). The level system is illustrated in Fig. 2a.

TABLE I Parameters of double branched Nd : glass laser system

Parameter	Branch GB1	Branch GB2	Reference
Resonator			
Output mirror	$R_1 = 0.7$	$R_2 = 0.7$	
Antiresonant mirror	$R_{HM} = 0.5$	$R_{HM} = 0.5$	
Round-trip time (ns)	$T_R = 10$	$T_R = 10$	
Linear losses	$T_{lin} = 0.9$	$T_{lin} = 0.9$	
Solid angle (sr)	$\Delta\Omega = 5.6 \times 10^{-6}$	$\Delta\Omega = 5.6 \times 10^{-6}$	
Total flash duration (ms)	$T_{pu} = 1.5$	$T_{pu} = 1.5$	
Active medium			
Type	Schott LG760	Schott LG680	
Pumped rod length (cm)	$l_{G,1} = 10$	$l_{G,2} = 10$	
Nd^{3+}-concentration (cm^{-3})	$N_{G0} = 2.79 \times 10^{20}$	$N_{G0} = 2.79 \times 10^{20}$	[70]
Selected wavelength (nm)	$\lambda_1 = 1053.5$	$\lambda_2 = 1066.1$	
Selected wavenumber (cm^{-1})	$\nu_1 = 9492$	$\nu_2 = 9380$	
Emission cross-section (cm^2)	$\sigma_{G,1} = 4.2 \times 10^{-20}$	$\sigma_{G,2} = 2.5 \times 10^{-20}$	[70]
Fluorescence quantum efficiency	$\eta_1 = 0.94$	$\eta_2 = 0.73$	[57]
Fluorescence lifetime (μs)	$\tau_{G,1} = 360$	$\tau_{G,2} = 300$	[70]
Branching ratio	$\beta_1 = 0.5$	$\beta_2 = 0.49$	[57]
Saturable absorber			
Type	Kodak no. 9860	Kodak no. 9860	
Absorption cross-section (cm^2)	$\sigma_{A,1} = 3.65 \times 10^{-16}$	$\sigma_{A,2} = 3.7 \times 10^{-16}$	[51]
Effective emission cross-section (cm^2)	$\sigma_{E,1} = 1.3 \times 10^{-16}$	$\sigma_{E,2} = 1.8 \times 10^{-16}$	[52]
Recovery time (ps)	$\tau_A = 7$	$\tau_A = 7$	[71]
Small-signal transmission	$T_{A0,1} = 0.5$	$T_{A0,2} = 0.495$	
Focusing factor	$f_{foc} = 3$	$f_{foc} = 3$	
Q-switch			
Opening time position (μs)	$t_{Q1} = 800$	$t_{Q2} = 800$	
Pre-Q-switch transmission	$T_{pre,1} = 0.5$	$T_{pre,2} = 0.5$	
After-Q-switch transmission	$T_{aft,1} = 1$	$T_{aft,2} = 1$	
Acoustooptic modulator			
Modulation frequency (Hz)	$\nu_{AOM} = 5 \times 10^7$	$\nu_{AOM} = 5 \times 10^7$	
Modulation factor	$\delta_{AOM} = 2$	$\delta_{AOM} = 2$	
Displacement (cm)	$\xi = 10$	$\xi = 10$	
Initial conditions at moment of Q-switch opening (Equation 7)			
Spike duration (ps)	$t_0 = 2.1$	$t_0 = 2.1$	
Time positions (ns)	$t_a = 4.92$, $t_c = 5.08$	$t_b = 5$	
Relative heights	$\kappa_a = 4$, $\kappa_c = 3.65$	$\kappa_b = 4$	

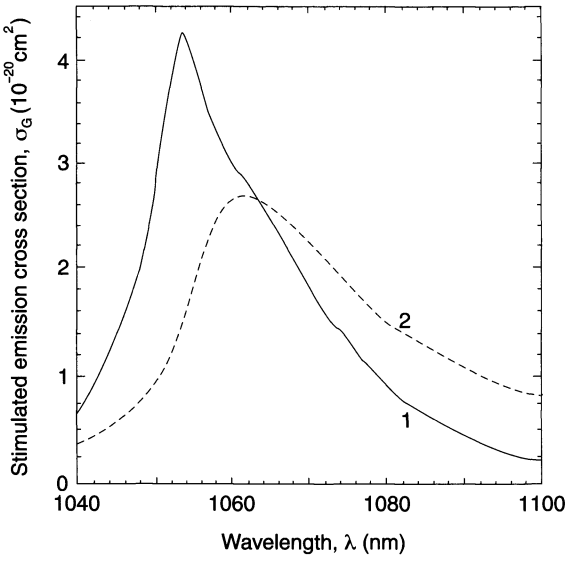

Figure 3 Stimulated emission cross-section spectra $\sigma_G(\lambda)$ of gain media. Solid curve 1, Nd : phosphate laser glass Schott LG760 (from [50]). Dashed curve 2, Nd : silicate laser glass Schott LG680 (from [50]).

The spectroscopic data of the Schott laser glasses LG760 (Nd : phosphate glass) and LG680 (Nd : silicate glass) are used in the simulations. Relevant parameters are collected in Table I. The stimulated emission cross-section spectra of the laser glasses applied have been determined previously [50] and are displayed in Fig. 3.

The saturable absorber is described by the level system of Fig. 2b. The spectroscopic data of Kodak dye no. 9860 are applied. The relevant parameters are collected in Table I. The ground-state absorption cross-section spectrum $\sigma_A(\lambda)$ [51] and the stimulated emission cross-section spectrum of thermally relaxed molecules in the S_1 state $\sigma_E(\lambda)$ [52] are shown in Fig. 4. The absorption cross-section spectrum $\sigma_A(\lambda)$ of the thermally populated ground-state levels

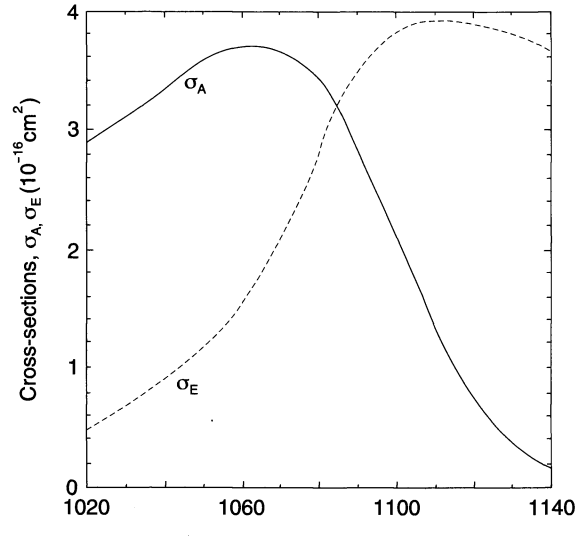

Figure 4 Absorption cross-section spectrum $\sigma_A(\lambda)$ (solid curve, from [51]) and stimulated emission cross-section spectrum $\sigma_E(\lambda)$ (dashed curve, from [52]) of mode-locking dye Kodak no. 9860.

overlaps with the stimulated emission cross-section spectrum $\sigma_E(\lambda)$ of the thermally relaxed molecules in the S_1 state. A fast relaxation out of the Franck–Condon states of absorption and emission is assumed. A more detailed description must use a multilevel system and include spectral cross-relaxation [53, 54]. It should be noted that in the saturable absorber medium the propagating pulses are coupled by population-dependent absorption and emission. The synchronization action of the saturable absorption is acting not only if both pulses are in the absorption region, but also if one pulse causes an S_1 state excitation in the absorption region and the other pulse is amplified in the stimulated emission region by the generated S_1 state population.

The temporal light transmission through the acoustooptic modulator–antiresonant ring arrangement is given by [55]

$$T_{AOM}(t') = R_{HM}(1 - R_{HM})\left\{\cos\left[\delta_M \sin\left(2\pi\nu_{AOM}\left(\frac{T_R}{2} + t' - \frac{\xi}{c_0}\right)\right)\right] + \cos\left[\delta_M \sin\left(2\pi\nu_{AOM}\left(\frac{T_R}{2} + t' + \frac{\xi}{c_0}\right)\right)\right]\right\}^2 \quad (1)$$

where δ_M is the modulation index, ν_{AOM} is the modulator frequency, T_R is the resonator round-trip time, t' is the time, ξ is the displacement of the modulator (fused silica) out of the middle of the antiresonant ring, and R_{HM} is the reflectivity of the antiresonant ring mirror HM. The modulation index depends on the RF drive power P_A by $\delta_M = \kappa P_A^{1/2}/\lambda$ ($\kappa = 9.5 \times 10^{-7}\,W^{-1/2}\,m$ for our arrangement [56]). A $T_{AOM}(t')$ curve is displayed in Fig. 5 for $\delta_M = 2$ ($P_A = 4.9\,W$).

The double pulse development in the pre-Q-switch region is simulated by Equations 2 to 6.

$$J_{i,j} = J_{0,i} \sin\left(\pi \frac{jT_R}{T_{pu}}\right) \quad (2)$$

$$N_{G3,i,j+1} = N_{G3,i,j} + J_{i,j}\frac{N_{G1,i,j}}{N_{G0,i}}T_R - \frac{T_R}{\tau_{sp,i}}N_{G3,i,j} - \frac{\sigma_{G,i}}{h\nu_i}N_{G3,i,j}w_{G,i,j} \quad (3)$$

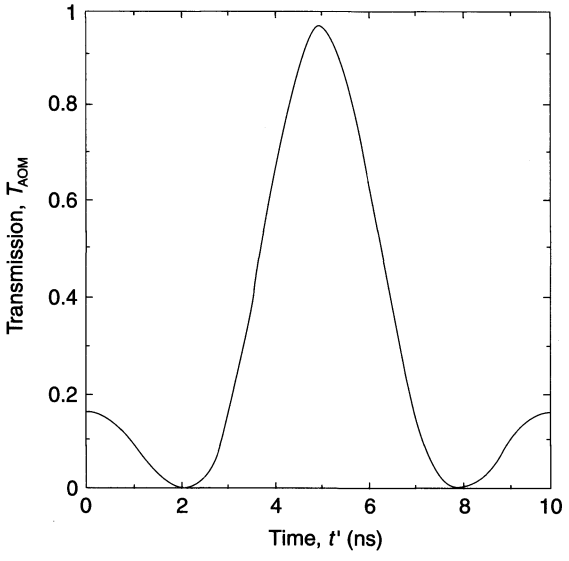

Figure 5 Transmission through antiresonant ring with acoustooptic modulator (Equation 1). Data of Table I are applied. Modulation index $\delta_M = 2$. Displacement $\xi = 10\,cm$.

$$N_{\mathrm{G1},i,j} = N_{\mathrm{G0},i} - N_{\mathrm{G3},i,j} \tag{4}$$

$$I_{\mathrm{G},i,j+1}(t') = I_{\mathrm{G},i,j}(t') \exp(\sigma_{\mathrm{G},i} N_{\mathrm{G3},i,j} l_{\mathrm{G},i}) T_{\mathrm{Q},j} T_{\mathrm{AOM}}(t') T_{\mathrm{A},i,j}(t') R_i T_{\mathrm{lin}} + \frac{h\nu_i}{\tau_{\mathrm{sp},i}} \eta_i \beta_i \frac{\Delta\Omega}{4\pi} l_{\mathrm{G},i} N_{\mathrm{G3},i,j} \tag{5}$$

$$w_{\mathrm{G},i,j} = \int_0^{T_\mathrm{R}} I_{\mathrm{G},i,j}(t)\,\mathrm{d}t \tag{6}$$

where i is the branch index and j counts the number of round-trips in the pre-Q-switch region. The initial conditions of the level populations of the gain media are (Fig. 2a) $N_{\mathrm{G1},i,0} = N_{\mathrm{G0},i}$, $N_{\mathrm{G2},i,0} = N_{\mathrm{G3},i,0} = N_{\mathrm{G4},i,0} = 0$. $N_{\mathrm{G0},i}$ is the total number density of active ions. The initial conditions of the laser intensities are $I_{\mathrm{G},i,0} = 0$. R_i is the reflectivity of the output mirror of branch i. T_{lin} takes into account linear transmission losses in the cavities. η_i is the luminescence quantum yield of the upper laser level and β_i is the fraction of spontaneous emission terminating in the lower laser level (branching ratio) [57]. $\Delta\Omega$ is the solid angle of effective amplified spontaneous emission ($\Delta\Omega \approx \pi\Delta\theta^2/4$ where $\Delta\theta$ is the full divergence angle of the laser beam). Equation 2 describes the pump rate of the flash lamps. Equation 3 gives the upper laser level population density at round-trip number $j+1$. The population density is averaged over one round-trip period. The second term of Equation 3 gives the population by the pump light, where the factor $N_{\mathrm{G1},i,j}/N_{\mathrm{G0},i}$ takes care of depletion of the ground-state population of the gain medium by the pump flash. The third term describes the spontaneous and non-radiative decay, and the last term gives the level depopulation by stimulated emission. Equation 5 handles the increase of the laser light per round-trip. The first term gives the effective amplification per round-trip including stimulated emission and various transmission losses, while the second term gives the spontaneous emission contribution. $T_Q = T_{\text{pre-}Q}$ is the transmission through the Q-switch Pockels cell in the pre-Q-switch region. $T_{\mathrm{A},i}(t') = T_{\mathrm{A0},i}$ is the small-signal transmission of the saturable absorber. $w_{\mathrm{G},i,j}$ (Equation 6) is the pulse energy density in laser branch i for round-trip number j.

After the Q-switch has opened, the pulse development is speeded up rapidly and the saturable absorption dynamics has to be included in the pulse development. The temporal fluctuation structure of the laser light after the pre-Q-switch has to be taken into account to describe the picosecond pulse generation by the passive saturable absorber action. The temporal fluctuations result from the broad-band spontaneous emission (Gaussian noise characteristics [44, 58]). These fluctuations are amplified linearly in the pre-Q-switch region. Only a temporal broadening occurs by the spectral filtering action of the active medium (natural mode selection by finite spectral gain width [44, 58]) and of the spectral tuning filters (T1 and T2 in Fig. 1). For our numerical simulations the Gaussian noise statistics are neglected in the pre-Q-switch region (envelope amplification is considered). But they are approximately considered in the after-Q-switch regime by modifying the temporal intensity distributions at the moment of Q-switching from $I_i(t')$ to $I_i(t')s_i(t')$ where

$$s_1(t') = \frac{1 + \kappa_\mathrm{a} \exp[-(t'-t_\mathrm{a})^2/t_0^2] + \kappa_\mathrm{c} \exp[-(t'-t_\mathrm{c})^2/t_0^2]}{1 + (1/T_\mathrm{R}) \int_0^{T_\mathrm{R}} \{\kappa_\mathrm{a} \exp[-(t''-t_\mathrm{a})^2/t_0^2] + \kappa_\mathrm{c} \exp[-(t''-t_\mathrm{c})^2/t_0^2]\}\,\mathrm{d}t''} \tag{7a}$$

$$s_2(t') = \frac{1 + \kappa_\mathrm{b} \exp[-(t'-t_\mathrm{b})^2/t_0^2]}{1 + (1/T_\mathrm{R}) \int_0^{T_\mathrm{R}} \kappa_\mathrm{b} \exp[-(t''-t_\mathrm{b})^2/t_0^2]\,\mathrm{d}t''} \tag{7b}$$

The denominators in Equations 7a and 7b keep the energy content constant. The radiation in branch GB1 is modified by two spikes of relative height κ_a and κ_c at the temporal positions t_a and t_c. The radiation in branch GB2 is modified by one spike of relative height κ_b at position t_b. t_0 is half of the 1/e width of the spikes. κ_a and κ_c represent the enhancement factors of the highest and second-highest spikes above the average spike light (envelope intensity $I_1(t')$ used in the pre-Q-switch region) of the radiation in branch GB1. κ_b gives the enhancement factor of the highest spike in branch GB2. The parameters applied in the simulations are listed in Table I. They are rationalized by the following considerations. A spectral bandwidth of $\Delta\tilde{\nu}_{ini} \approx 5\,cm^{-1}$ is assumed at the end of the pre-Q-switch phase corresponding to a fluctuation duration of $\Delta t_{ini} \approx 0.5/(c_0\,\Delta\tilde{\nu}_{ini}) \approx 3.5$ ps and $t_0 = \Delta t_{ini}(\ln 2)^{-1/2}/2 = 2.1$ ps. The intensity envelope at the end of the pre-Q-switch phase is approximately $\Delta t_{env} \approx 1$ ns. The number of fluctuations within the envelope is $m \approx \Delta t_{env}/(2\,\Delta t_{ini}) \approx 143$. The peak intensity of the highest spike is $I_a = (1+\kappa_a)I_{env} = \ln(m)I_{env} \approx 5I_{env}$ [44] ($\kappa_a = \kappa_b = 4$), and the peak intensity of the second-highest peak is given by $I_c = (1+\kappa_c)I_{env} = I_{env}[\ln(m) + \ln(m/2)]/2 \approx 4.65I_{env}$ [44] ($\kappa_c = 3.65$).

The simulated spike structure represents a worst-case situation for the temporal synchronization of the radiation in branch GB1 and branch GB2, since the earlier spike a is higher than the later spike c in branch GB1 (strongest absorption acting on most intense spike) and the spikes a and c of branch GB1 are widely separated from the spike b of branch GB2. Since the spikes are selected so that a worst-case situation is considered for the pulse synchronization, in our real experiments the pulse synchronization of both cavities is at least as good as calculated in the simulations. The Gaussian noise could have been simulated numerically by applying a noise generator. But then in each computer run a different noise pattern would have been generated, which would make it difficult to clarify the influences of various parameters in the computer runs. Additionally the restriction to three spikes drastically reduces the computation time and the necessary computer memory.

Equations 2 to 6 remain valid in the after-Q-switch regime and the saturable absorption dynamics are described by Equations 8 to 12.

$$I_{A,i,j'}(t', z=0) = f_{foc}\, I_{G,i,j'}(t') \tag{8}$$

$$\frac{\partial N_{S0,j'}}{\partial t'} = -\left(\frac{\sigma_{A,1}}{h\nu_1} I_{A,1,j'}(0) + \frac{\sigma_{A,2}}{h\nu_2} I_{A,2,j'}(0)\right) N_{S0,j'} + \left(\frac{\sigma_{E,1}}{h\nu_1} I_{A,1,j'}(0) + \frac{\sigma_{E,2}}{h\nu_2} I_{A,2,j'}(0)\right) N_{S1,j'} + \frac{N_{S1,j'}}{\tau_A} \tag{9}$$

$$\frac{\partial N_{S1,j'}}{\partial t'} = \left(\frac{\sigma_{A,1}}{h\nu_1} I_{A,1,j'}(0) + \frac{\sigma_{A,2}}{h\nu_2} I_{A,2,j'}(0)\right) N_{S0,j'} - \left(\frac{\sigma_{E,1}}{h\nu_1} I_{A,1,j'}(0) + \frac{\sigma_{E,2}}{h\nu_2} I_{A,2,j'}(0)\right) N_{S1,j'} - \frac{N_{S1,j'}}{\tau_A} \tag{10}$$

$$I_{A,i,j'}(t', l_A) = I_{A,i,j'}(t', 0) \exp\{[-\sigma_{A,i} N_{S0,j'} + \sigma_{E,i} N_{S1,j'}] l_A\} \tag{11}$$

$$T_{A,i,j'}(t') = \frac{I_{A,i,j'}(t', l_A)}{I_{A,i,j'}(t', 0)} \tag{12}$$

Here the index j' counts the number of round-trips in the after-Q-switch region. Equation 8 transfers the intensity in the gain branches to the intensity at the absorber medium in the

antiresonant ring. The focusing factor f_{foc} takes into account spatial beam profile narrowing (factor of 2, curvature of output mirrors is $\rho = 3\,m$), pulse splitting at the antiresonant ring mirror (factor of 0.5), and the intensity enhancement of the colliding pulses in the absorber cell (factor of 3 [59]). Equations 9 and 10 apply to the saturable absorber model of Fig. 2b. The first terms describe the ground-state depopulation by ground-state absorption, the second terms consider ground-state refilling by stimulated emission from the thermally relaxed population in the S_1 state, and the third terms give the S_1 state level depopulation by spontaneous emission and nonradiative decay. Equation 11 is obtained by neglecting the variation of the level populations along the pulse propagation direction through the absorber cell of length l_A (optically thin saturable absorber limit [60]). This approximation saves computing time.

3. Simulations

In the following, computer simulations of the pulse development under various conditions are presented. The applied parameters are listed in Table I. First the single pulse development is studied (one of the gain media is not pumped) under active mode-locked condition ($T_{A,0} = 1$), and active and passive mode-locked condition ($T_{A,0} = 0.5$). Then the same operation modi are studied in the case of double pulse operation (both gain media are pumped) and the temporal synchronization of both laser branches is analysed.

3.1. Single-branch operation

The separate operation of the Q-switched and mode-locked Nd:phosphate glass laser (index $i = 1$, branch GB1 and antiresonant ring ARR) and of the Q-switched and mode-locked Nd:silicate glass laser (index 2, branch GB2 and antiresonant ring ARR) is investigated. The parameters of Table I are applied.

The initial gain, $G_{0,i} = I_{G,i,j'=1}(t' = T_R/2)/I_{G,i,j'=0}(t' = T_R/2)$, after Q-switch opening versus pump rate J is displayed in Fig. 6. The situations $T_{A,0} = 1$ (dashed curves 1 and 2, pure active mode-locking) and $T_{A,0} = 0.5$ (solid curves 1 and 2, hybrid mode-locking) are considered. The pump rates J giving $G_0 = 1$ are the laser pump rate thresholds. Above threshold the initial gain increases slightly more strongly than linearly.

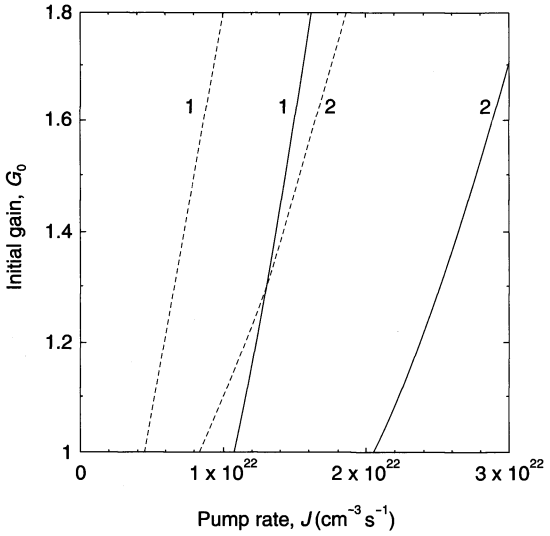

Figure 6 Initial gain G_0 after Q-switch opening versus pump rate J. Dashed curves, active mode-locked system ($T_{A,0} = 1$). Solid curves, hybrid mode-locked system with small-signal saturable absorber transmission of $T_{A,0} = 0.5$. Curves 1, Nd:phosphate glass branch GB1; curves 2, Nd:silicate glass branch GB2. Data of Table I are applied.

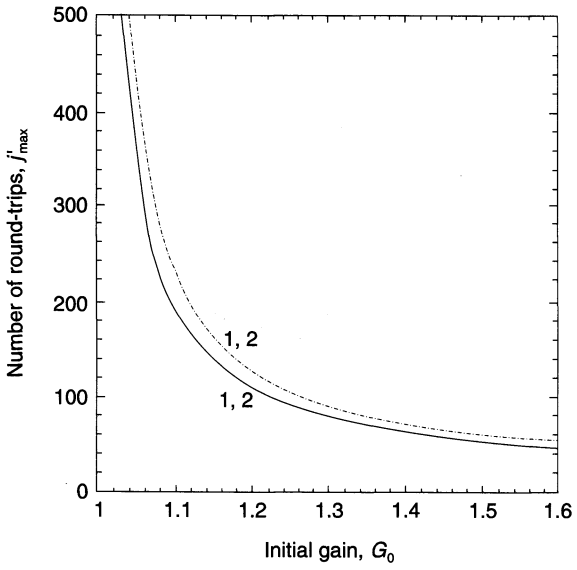

Figure 7 Round-trip number $j'_{max} = (t_{max} - t_Q)/T_R$ at pulse train maximum versus initial gain G_0. t_{max} is temporal position of pulse train maximum. t_Q is temporal position at moment of Q-switch opening. Single laser operation is considered. Data of Table I are applied. Dash-dotted curve, active mode-locked system ($T_{A,0} = 1$). Solid curve, hybrid mode-locked system ($T_{A,0} = 0.5$). Curve 1 for Nd : phosphate glass branch and curve 2 for Nd : silicate glass branch coincide.

3.1.1. Q-switching and active mode-locking

The Q-switched and active mode-locked laser performance ($T_A = 1$) is illustrated by the dash-dotted curves 1 (branch GB1) and 2 (branch GB2) in Figs 7 to 10. The temporal fluctuations are neglected for this analysis ($s_1(t') = s_2(t') = 1$, see Equations 7a and 7b).

The round-trip number j'_{max} of the pulse train maximum in the after-Q-switch region versus initial gain G_0 is shown in Fig. 7. $j'_{max,1}$ and $j'_{max,2}$ coincide (only one curve). The build-up time decreases rapidly with rising initial gain G_0.

The peak intensity I_G at the pulse train maximum versus initial gain G_0 is shown by the dash-dotted curves 1 and 2 in Fig. 8. I_G increases roughly linearly with G_0. The peak intensities in the

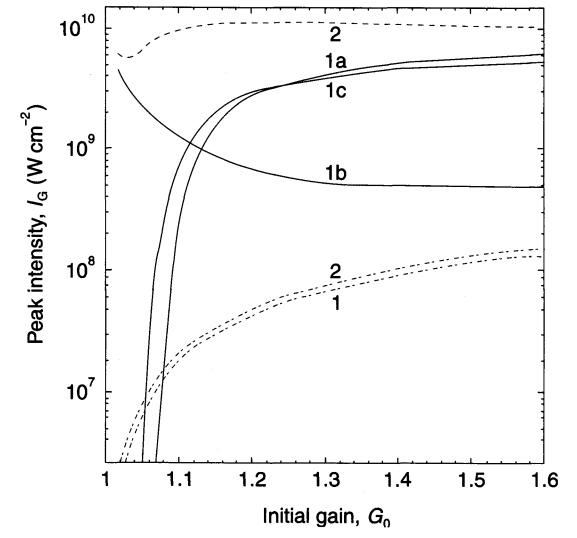

Figure 8 Peak intensity I_G in gain branch region at pulse train maximum j'_{max} versus initial gain G_0. Single gain branch operation is considered. Dash-dotted curves, active mode-locked system ($T_{A,0} = 1$). Solid and dashed curves, hybrid mode-locked system ($T_{A,0} = 0.5$). Curves 1, Nd : phosphate glass branch. Curves 2, Nd : silicate glass branch. a, b, and c indicate time positions within one resonator round-trip (Equation 7). Data of Table I are applied.

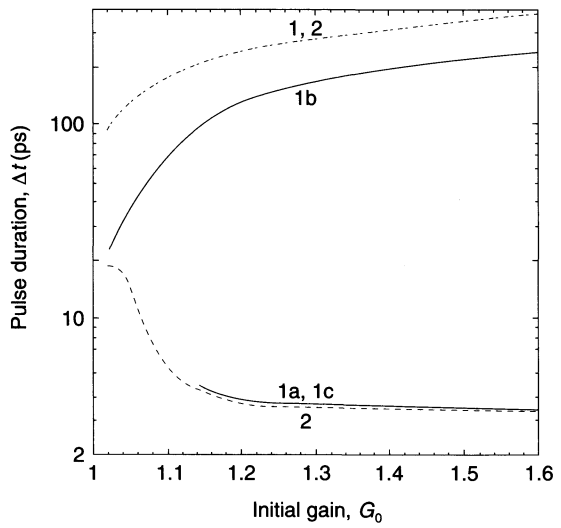

Figure 9 Pulse duration Δt (FWHM) at pulse train maximum versus initial gain G_0. Legend of Fig. 8 applies.

Nd : silicate glass branch GB2 are approximately a factor of 1.15 higher than in the Nd : phosphate glass branch GB1.

The pulse duration Δt (FWHM) at the pulse train maximum versus initial gain G_0 is shown by the dash-dotted curve in Fig. 9. Δt_1 and Δt_2 coincide (only one curve). The pulse duration is determined by the action of the acoustooptic modulator (transmission half-width is 2.5 ns, see Fig. 5). The pulse durations shorten with decreasing initial gain (elongation of build-up time, Fig. 9). At $G_0 = 1.02$ ($j'_{max} = 850$) the pulse duration obtained is $\Delta t = 96$ ps, while for $G_0 = 1.5$ the calculated pulse duration is $\Delta t = 350$ ps.

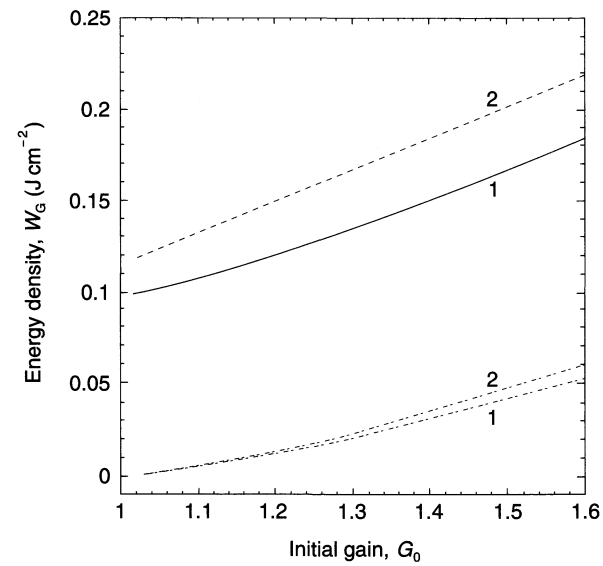

Figure 10 Circulating energy density w_G in gain branch at pulse train maximum versus initial gain G_0. Single gain branch operation is considered. Dash-dotted curves, $T_{A,0} = 1$. Solid and dashed curves, $T_{A,0} = 0.5$. Curves 1, gain branch GB1. Curves 2, gain branch GB2. Data of Table I are applied.

The energy density of the circulating radiation w_G (Equation 6) in the gain branch at the pulse train maximum versus initial gain G_0 is displayed by the dash-dotted curves in Fig. 10. The energy density of the Nd : silicate glass laser is approximately a factor of 1.15 higher than the energy density of the Nd : phosphate glass laser.

The dash-dotted curves presented in Figs 7 to 10 were calculated for an Nd : silicate and an Nd : phosphate gain medium, but the illustrated tendencies of round-trip numbers, peak intensities, pulse durations, and energy densities versus initial gain apply generally to active mode-locked lasers.

3.1.2. Q-switching and hybrid mode-locking

The Q-switched and hybrid mode-locked (acoustooptic modulator and saturable absorber with $T_{A,0} = 0.5$) laser performance is included in Figs 7 to 10. The temporal spiking is taken into account approximately (Equations 7a and 7b).

The solid curve in Fig. 7 displays the number of round-trips j'_{max} in the after-Q-switch range at the pulse train maximum. $j'_{max,1}$ and $j'_{max,2}$ coincide (only one curve). The build-up time shortens drastically with increasing pump rate (initial gain G_0).

In Fig. 8 the dependence of the peak intensity of the pulses I_G at the pulse train maximum is considered. The dashed curve 2 belongs to the Nd : silicate glass laser (initial intensity distribution of Equation 7b). One spike at the transmission maximum of the acoustooptic modulator was applied and the intensity peak remains at this position. Over a wide initial gain range the peak intensity $I_{G,2}$ remains constant. For the applied initial intensity distribution of the Nd : phosphate glass laser (Equation 7a), the development of the peaks a, b and c is considered. Initially spike a is most intense. It remains the highest spike at the pulse train maximum for initial gains $G_0 \geq 1.24$ (curve 1a). The second-highest initial spike c dominates in the range $1.115 \leq G_0 \leq 1.24$ (curve 1c). The leading edge absorption of the saturable absorber attenuates the first spike more strongly than the second spike. For weak initial gains ($G_0 \leq 1.115$, long build-up time, elongated nonlinear saturable absorption action) the leading edge absorption of the saturable absorber reduces the two spikes and the intensity distribution at the transmission maximum of the acoustooptic modulator becomes dominant (curve 1b). The curves 1a, 1b and 1c show that for laser operation slightly above threshold the saturable absorber action is most active and single pulse operation is achieved by efficient background suppression.

The development of the pulse durations is shown by the dashed and solid curves in Fig. 9. At high initial gains the initial pulse durations are only slightly modified by the saturable absorber action. In the range $1.03 \leq G_0 \leq 1.2$, the pulse duration for the Nd : silicate glass laser (dashed curve 2, intensity distribution of Equation 7b) increases with decreasing G_0 because of the spike removal by the transient slow saturable absorber action of the mode-locking dye ($\tau_A = 7$ ps, initial spike duration $\Delta t_{ini} = 2(\ln 2)^{1/2} t_0 = 3.5$ ps). In the region $1 \leq G_0 \leq 1.03$, pulse shortening occurs with decreasing gain (the broad pedestal pulse is shortened). The solid curves 1a, 1c (coinciding) and 1b belong to the pulse durations at the pulse train maximum of the Nd : phosphate glass laser (intensity distribution of Equation 7a). The pulse duration of the spikes a and c (curves 1a, 1c) behave similarly to curve 2. Only for $G_0 \leq 1.13$ have the spikes died out. Curve 1b shows the development of the pedestal intensity distribution. The pulse duration shortens with decreasing initial gain. A comparison of the solid curve 1b with the dash-dotted curve 1 shows the pulse-shortening action of the saturable absorber.

The energy densities of the circulating pulses w_G at the train maximum are shown by the dashed and solid curves in Fig. 10. The energy density of the Nd : silicate glass laser is approximately a factor of 1.2 larger than the energy density of the Nd : phosphate glass laser.

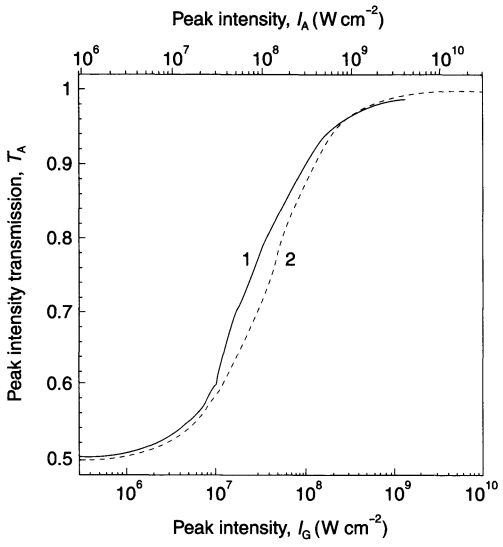

Figure 11 Peak intensity transmission T_A through mode-locking dye versus peak intensity in gain branch (lower abscissa) and peak intensity at saturable absorber cell (upper abscissa) along the pulse train build-up. Single-branch operation. Initial gain $G_0 = 1.1$. Solid curve 1, Nd : phosphate glass branch (steep rise at $I_G = 10^7\,\mathrm{W\,cm^{-2}}$ due to change of highest intensity position from c to b). Dashed curve 2, Nd : silicate glass branch. Data of Table I are applied.

In Fig. 11 the nonlinear transmission behaviour of the saturable absorber along the developing pulse train intensity is illustrated. The curves belong to $G_0 = 1.1$. The peak intensity transmission T_A versus peak pulse intensity is shown for the Nd : phosphate glass laser (GB1) by the solid curve 1 and for the Nd : silicate glass laser (GB2) by the dashed curve 2 (it should be noted that $I_A = f_{foc} I_G = 3I_G$). The kick in curve 1 at $I_G = 1 \times 10^7\,\mathrm{W\,cm^{-2}}$ occurs where the intensity distribution at position b becomes higher than at position c.

The dashed and solid curves in Figs 7 to 10 were calculated for an Nd : silicate and an Nd : phosphate gain medium and the saturable absorber Kodak dye no. 9860, but the tendencies of the curves for the number of round-trips, the peak intensities, the pulse durations and the energy densities versus initial gain apply quite generally to hybrid mode-locked lasers.

3.2. Double-branch operation

The simultaneous operation of both laser branches is studied in this section. The applied parameters are listed in Table I. In all studies Q-switching is applied to start laser action at the same moment in both branches. The situations of active mode-locking and hybrid mode-locking are studied in the following. The results are compared to single-pulse operation (Section 3.1).

3.2.1. Q-switching and active mode-locking

The common electrooptic Q-switch guarantees the simultaneous start of laser action in both branches, and the common acoustooptic modulator guarantees the temporal synchronization of both pulse trains (same loss modulation, see Fig. 5). There is no coupling of both lasers (like master–slave operation). Each laser part gives the same output in the simultaneous pumping mode as in the separate pumping mode. The laser performance curves shown by the dash-dotted curves in Figs 7 to 10 also apply to the simultaneous two-branch operation.

The dash-dotted curves in Figs 7 to 10 indicate that the pulse trains in both gain branches need the same number of round-trips for the pulse train maximum, they obtain nearly the

same peak intensity and energy density and they get the same pulse duration if the initial gain is the same. In the case of low initial gain $G_0 < 1.1$, the build-up time depends strongly on the actual G_0 value, and a slight difference between $G_{0,1}$ and $G_{0,2}$ would lead to a loss of pulse train synchronization (simultaneous occurrence of pulse train maxima for both branches). These theoretical findings are in good agreement with experimental results [39] where the build-up time and build-up time jitter as a function of flash lamp pump voltage were measured.

3.2.2. Q-switching and hybrid mode-locking

The incorporation of the saturable absorber action to the two-branch laser operation leads to a nonlinear coupling of both systems (mutual master–slave interaction). This master–slave coupling leads to a temporal synchronization of the emission within the opening window of the acoustooptic modulator. It causes a nearly simultaneous occurrence of the pulse train maxima and a temporal locking of the pulses in both branches even in the case of slightly different initial gains $G_{0,1}$ and $G_{0,2}$.

The double pulse laser performance is illustrated in Figs 12 to 16. In Figs 12 and 13 the peak intensity and the pulse duration at the pulse train maximum versus initial gain are displayed, respectively, for the case of equal initial gain in both branches, i.e. $G_{0,2}/G_{0,1} = 1$. Figure 12a shows the peak intensities of branch GB1 (initial intensity distribution of Equation 7a). The peak 1b dominates for $G_{0,1} < 1.31$. The dominance of peak 1b is enhanced by the master action of the pulse 2b (saturable absorber bleaching of pulse 2b) as is seen by comparison with Fig. 8. In Fig. 12b the dominance of pulse 2b is clearly seen. The build-up of the pulses 2a and 2c by the master action of the pulses 1a and 1c in the region of high initial gain is displayed by the corresponding curves. For $G_0 < 1.31$ the temporal synchronization of the radiation in branch GB1 and branch GB2 is achieved since the pulses 1b and 2b are dominant and occur at the same time (locking to the same time position independent of the initial spike distribution). For $G_0 > 1.31$ the temporal synchronization of the radiation in branch GB1 and branch GB2 is lost since in branch GB1 the pulses 1a and 1c are dominant while in branch GB2 the pulse 2b is dominant (locking of the initially independent fluctuations in both branches to the same time position is not achieved). The pulse duration curves in Fig. 13 show the mutual

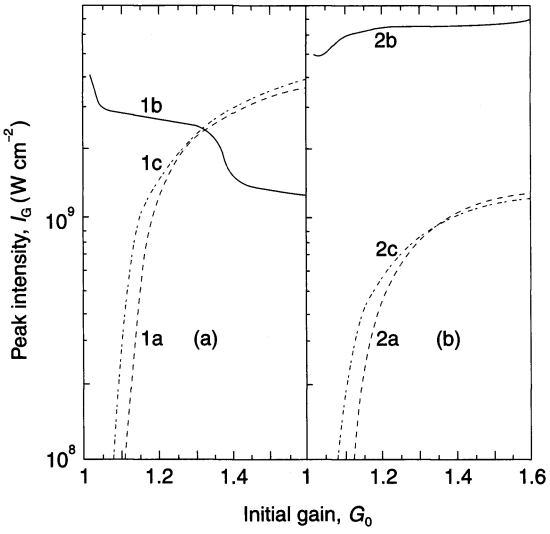

Figure 12 Dependence of spike intensities in gain branch $I_{G,\mu}$, at pulse train maximum on initial gain G_0 ($G_{0,1} = G_{0,2}$). μ = a, b, c are time positions defined by Equation 7. Hybrid mode-locked double-pulse laser operation. Data of Table I apply. (a) Nd : phosphate glass branch with initial intensity distribution of Equation 7a. (b) Nd : silicate glass branch with initial intensity distribution of Equation 7b.

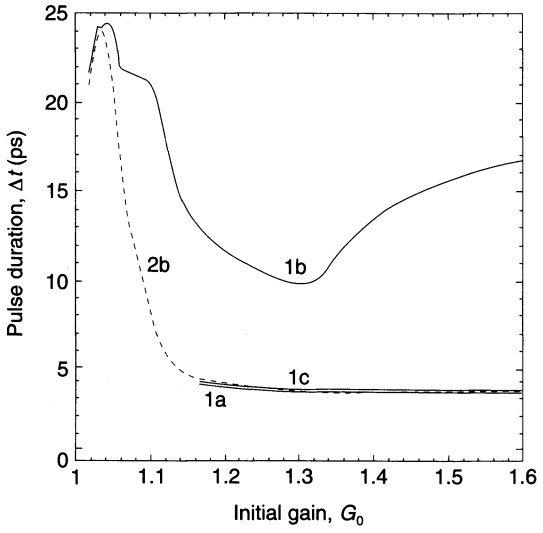

Figure 13 Dependence of spike pulse durations, Δt_μ (μ = a, b, c), at pulse train maximum on initial gain G_0 ($G_{0,1} = G_{0,2}$). Hybrid mode-locked double pulse laser operation. Data of Table I apply. Solid curves 1a, 1b and 1c, Nd:phosphate glass branch with initial intensity distribution of Equation 7a (spikes a, c, and pedestal b at transmission maximum of acoustooptic modulator). Dashed curve 2b, Nd:silicate glass branch with initial intensity distribution of Equation 7b (spike b).

master–slave coupling effect by comparison with the curves in Fig. 9. The duration of the initially long pulse 1b is drastically shortened while the duration of the initially short pulse 2b is slightly elongated. The duration of the spikes 1a and 1c is only weakly influenced.

The influence of different initial gain in both branches is analysed in Figs 14 to 16. The initial gain of branch GB1 is fixed at $G_{0,1} = 1.1$ and the initial gain of the second branch GB2 is varied between 1.0175 and 1.2 ($0.925 \leq G_{0,2}/G_{0,1} \leq 1.09$). The difference in initial gain leads to a different build-up time and the round-trip numbers $j'_{\max,1}$ and $j'_{\max,2}$ for the pulse train maxima do not coincide. The interval $j'_{\max,2} - j'_{\max,1}$ between the pulse train maxima is displayed by the solid curve in Fig. 14 (stepping curve is smoothed out). The train maximum of branch GB2 occurs before the train maximum of branch GB1 for $G_{0,2} > G_{0,1}$ and vice versa for $G_{0,2} < G_{0,1}$. For comparison the dash-dotted curve displays the difference in the round-trip

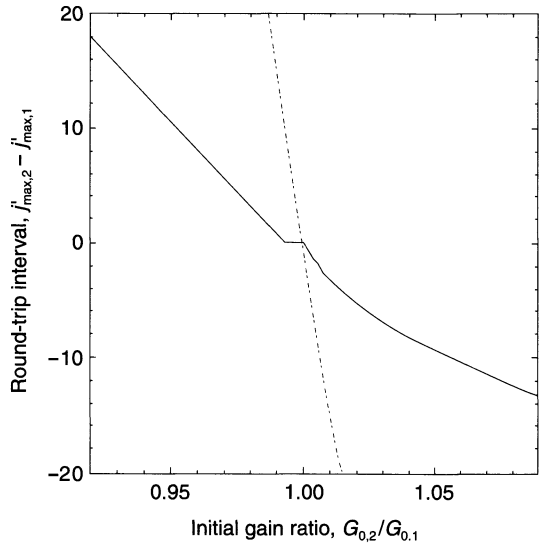

Figure 14 Dependence of interval of round-trips, $j'_{\max,1} - j'_{\max,2}$, between pulse train maxima on initial gain ratio $G_{0,2}/G_{0,1}$ for $G_{0,1} = 1.1$. Data of Table I apply. Solid curve, hybrid mode-locked double-pulse laser operation. Dash-dotted curve, separate operation of both branches.

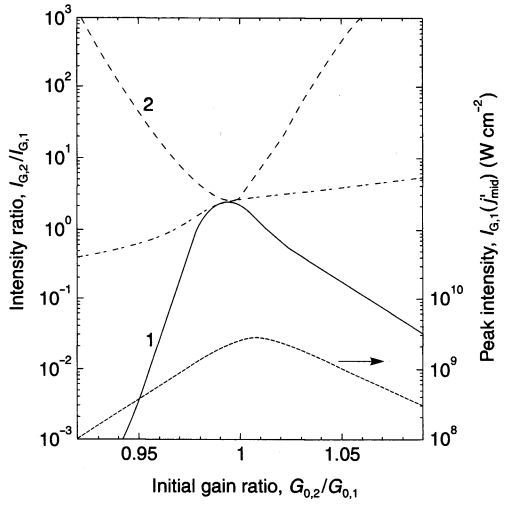

Figure 15 Dependence of peak intensity ratio $I_{G,2}/I_{G,1}$ on initial gain ratio $G_{0,2}/G_{0,1}$. Hybrid mode-locked double-pulse laser operation. $G_{0,1} = 1.1$. Data of Table I apply. Solid curve 1, $I_{G,2}/I_{G,1}$ at $j'_{max,1}$ (pulse train maximum in Nd : phosphate glass branch). Dashed curve 2, $I_{G,2}/I_{G,1}$ at $j'_{max,2}$ (pulse train maximum in Nd : silicate glass branch). Dash-dotted curve, $I_{G,2}/I_{G,1}$ at $j'_{mid} = (j'_{max,1} + j'_{max,2})/2$. The dotted curve shows $I_{G,1}(j'_{mid})$.

numbers $j'_{max,2}(G_{0,2}) - j'_{max,1}(G_{0,1})$ in the case of separate laser operation. The narrowing of the round-trip interval in the case of simultaneous operation of both branches is evident, showing clearly the mutual master–slave coupling effect.

In Fig. 15 the peak intensity ratio $I_{G,2}/I_{G,1}$ at the pulse train maximum of branch GB1 is shown by the solid curve 1, and $I_{G,2}/I_{G,1}$ at the pulse train maximum of branch GB2 is shown by the dashed curve 2. The dash-dotted curve gives the intensity ratio $I_{G,2}/I_{G,1}$ at $j'_{mid} = (j'_{max,1} + j'_{max,2})/2$, and the short-dashed curve gives $I_{G,1}(j_{mid})$. For the midway position between the pulse train maxima the variation of the intensity ratio $I_{G,2}/I_{G,1}$ and of the peak intensity $I_{G,1}(j'_{mid})$ may be tolerable in the range $0.95 \leq G_{0,2}/G_{0,1} \leq 1.05$.

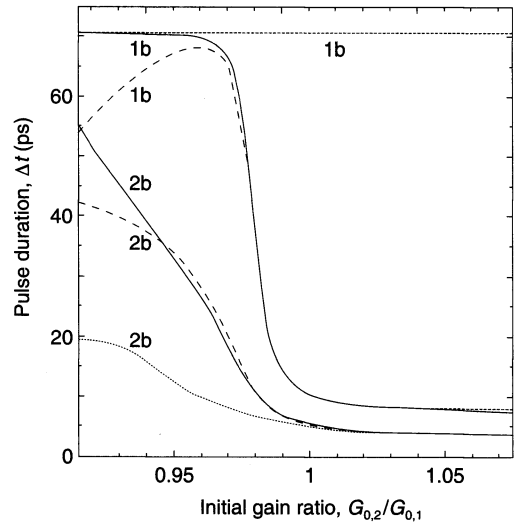

Figure 16 Dependence of pulse durations Δt on initial gain ratio $G_{0,2}/G_{0,1}$. Hybrid mode-locked double pulse laser operation. $G_{0,1} = 1.1$. Data of Table I apply. Curve 1b, pulses in gain branch GB1 at time position b. Curve 2b, pulses in gain branch GB2 at time position b. Solid curves 1b and 2b, Δt_1 and Δt_2 at $j'_{max,1}$. Dashed curves 1b and 2b, Δt_1 and Δt_2 at $j'_{max,2}$. The dotted curves 1b and 2b indicate the pulse durations in the case of separate operation of the gain branches GB1 and GB2.

The development of the pulse durations Δt_1 and Δt_2 at $j'_{\max,1}$ (solid curves) and $j'_{\max,2}$ (dashed curves) versus the initial gain ratio $G_{0,2}/G_{0,1}$ is shown in Fig. 16. The pulse durations in the case of separate laser operation are shown by the dotted curves 1b and 2b. For $G_{0,2} > G_{0,1}$ the branch GB1 is slave-locked to the branch 2 and the pulse durations Δt_1 (curves 1b) approach Δt_2 (curves 2b). For $G_{0,2} < G_{0,1}$ the branch GB2 is slave-locked to the branch GB1 and the pulse durations Δt_2 approach Δt_1 ($\Delta t_1(j'_{\max,2}) < \Delta t_1(j'_{\max,1})$ owing to continued pulse shortening in the trailing part of the pulse train).

4. Comparison with experimental results

The generation of time-synchronized frequency-tunable picosecond light pulses in a Q-switched active mode-locked and hybrid mode-locked Nd : glass double-branch laser system has been studied experimentally in a previous paper [39]. The theoretical findings of this paper are in full agreement with the experimental results.

In the case of active mode-locking, both laser branches had to be operated reasonably well above lasing threshold to get small temporal synchronization jitter. This is in agreement with the numerical simulations of Figs 7 to 10 in this paper. The temporal substructure within the pulse envelope of the active mode-locked laser may be avoided by spectral gain narrowing with a filter.

In the case of experimental hybrid mode-locking, the small-signal transmission of the saturable absorber had to be sufficiently small ($T_0 \approx 0.7$ was used) and both branches had to be operated only slightly above laser threshold to achieve pulses of approximately 15 ps duration with a synchronization jitter of approximately 5 ps. These experimental results are in good agreement with the numerical simulations of Figs 12 to 16 of this paper.

5. Conclusions

The performance of a branched double-pulse Nd : glass laser system has been analysed theoretically. Temporal synchronization was achieved by simultaneous laser starting (Q-switch-opening) active mode-locking, and saturable absorber passive mode-locking. The passive mode-locker in the antiresonant ring arrangement caused mutual master–slave time synchronization and pulse shortening. Previous experimental studies on a frequency-tunable time-synchronized Nd : phosphate glass and Nd : silicate glass double-branch laser system [39] are in good agreement with the numerical simulations presented here. The numerical simulations have been restricted to a single laser frequency for each branch, but the mutual master–slave coupling is active over the whole S_0–S_1 absorption range and the S_1–S_0 fluorescence range of the saturable absorber, allowing time-synchronized frequency tunable picosecond pulse generation over the full gain region of the Nd : phosphate and Nd : silicate glasses.

The numerical simulations presented of active mode-locking and hybrid mode-locking of a single laser are quite general. The results presented may therefore be applied to provide a feeling for active mode-locking and hybrid mode-locking of other laser systems.

The theoretical description presented of mutual master–slave coupled double-pulse laser operation may also be applied to other broad-band laser systems such as Ti : sapphire lasers ($Ti^{3+} : Al_2O_3$, tunable from 670 to 1100 nm) [61], $Cr^{3+} : LiSrAlF_6$ (Cr : LiSAF, tunable from 800 to 920 nm) [62], $Cr^{3+} : LiSr_{0.8}Ca_{0.2}AlF_6$ (Cr : LiSCAF, tunable from 800 to 880 nm) [63], $Cr^{3+} : LiCaAlF_6$ (Cr : LiCAF, tunable from 720 to 840 nm) [64], $Cr^{3+} : LiSrGaF_6$ (Cr : LiSGAF, tunable around 820 nm) [65], forsterite ($Cr^{4+} : Mg_2SiO_4$, tunable from 1.17 to 1.35 μm) [66–68], and $Cr^{4+} : YAG$ ($Cr^{4+} : Y_3Al_5O_{12}$, tunable from 1.37 to 1.51 μm) [69].

References

1. Y. R. SHEN, *The Principles of Nonlinear Optics* (Wiley, New York, 1984).
2. M. SCHUBERT and B. WILHELMI, *Nonlinear Optics and Quantum Electronics* (Wiley, New York, 1986).
3. A. LAUBEREAU, *Ultrashort Laser Pulses and Applications*, Topics in Applied Physics, Vol. 60, edited by W. Kaiser (Springer-Verlag, Berlin, 1988) p. 35.
4. Y. R. SHEN, *Prog. Quant. Electron.* **4** (1976) 207.
5. R. L. BYER and R. L. HERBST, *Nonlinear Infrared Generation*, edited by Y. R. Shen (Springer-Verlag, Berlin, 1977) p. 35.
6. F. ZERNIKE, *Methods of Experimental Physics*, Vol. XV: *Quantum Electronics, Part B*, edited by C. L. Tang (Wiley, New York, 1975) p. 143.
7. J. W. NIBLER and G. V. KNIGHTEN, *Raman Spectroscopy of Gases and Liquids*, edited by A. Weber (Springer-Verlag, Berlin, 1979) p. 253.
8. S. A. AKHMANOV, V. A. VYSLOUKH and A. S. CHIRKIN, *Optics of Femtosecond Laser Pulses* (American Institute of Physics, New York, 1992).
9. M. D. LEVENSON and S. S. KANO, *Introduction to Nonlinear Laser Spectroscopy*, revised edition (Academic Press, New York, 1988).
10. W. KAISER, editor, *Ultrashort Laser Pulses and Applications*, Topics in Applied Physics, Vol. 60 (Springer-Verlag, Berlin, 1988).
11. G. BEDDARD, *Rep. Prog. Phys.* **56** (1993) 63.
12. G. R. FLEMING, *Chemical Applications of Ultrafast Spectroscopy* (Oxford University Press, New York, 1986).
13. V. G. DIMITRIEV, G. G. GURZADYAN and D. N. NIKOGOSYAN, *Handbook of Nonlinear Optical Crystals* (Springer-Verlag, Berlin, 1991).
14. E. S. WACHMANN, W. S. PELOUCH and C. L. TANG, *J. Appl. Phys.* **70** (1991) 1893.
15. W. S. PELOUCH, P. E. POWERS and C. L. TANG, *Opt. Lett.* **17** (1992) 1070.
16. Q. FU, G. MAK and H. M. VAN DRIEL, *Opt. Lett.* **17** (1992) 1006.
17. A. PENZKOFER and W. KAISER, *Opt. Quantum Electron.* **9** (1977) 315.
18. R. R. ALFANO, editor, *The Supercontinuum Laser Source* (Springer-Verlag, New York, 1989).
19. A. PENZKOFER, A. BEIDOUN and H. J. LEHMEIER, *Opt. Quantum Electron.* **25** (1993) 349.
20. R. L. FORK, C. V. SHANK, C. A. HIRLIMANN and W. J. TOMLINSON, *Opt. Lett.* **8** (1983) 1.
21. A. MIGUS, A. ANTONETTI, J. ETCHEPARE, D. HULIN and A. ORZAG, *J. Opt. Soc. B* **2** (1985) 584.
22. M. HYDE and G. S. BEDDARD, *Chem. Phys.* **151** (1991) 239.
23. J. D. KAFKA, J. W. PIETERSE and M. L. WATTS, *Opt. Lett.* **17** (1992) 1286.
24. D. E. SPENCE, W. E. SLEAT, J. M. EVANS, W. SIBBETT and J. D. KAFKA, *Ultrafast Phenomena VIII*, Springer Series in *Chem. Phys.* **55**, edited by J. L. Martin, A. Migus, G. A. Mouro and A.H. Zewail (Springer-Verlag, Heidelberg, 1992) 194.
25. K. K. HOLSINGER, M. L. WATTS and J. D. KAFKA, *Conference on Lasers and Electro-Optics 1993*, Vol. 11, OSA Technical Digest Series (Optical Society of America, Washington, DC, 1993) p. 552.
26. L. S. GOLDBERG and C. A. MOORE, *Appl. Phys. Lett.* **27** (1975) 217.
27. J. P. HERITAGE and R. JAIN, *Appl. Phys. Lett.* **32** (1978) 101.
28. J. KUHL, *Appl. Phys. B* **28** (1982) 259.
29. H. LOBENTANZER, *Opt. Commun.* **71** (1989) 175.
30. U. SIEGNER, G. NOLL and E. O. GÖBEL, *Appl. Phys. B* **48** (1989) 21.
31. J. M. CLEMENS, J. NAJBAR, I. BRONSTEIN-BONTE and R. M. HOCHSTRASSER, *Opt. Commun.* **47** (1983) 271.
32. R. SCHEPS and J. F. MYERS, *IEEE Photon. Technol. Lett.* **4** (1992) 1.
33. S. G. BARTOSHEVICH, I. V. MIKHNYUK, G. A. SKRIPKO and I. G. TARAZEVICH, *IEEE J. Quantum Electron.* **27** (1991) 2234.
34. A. M. JOHNSON and W. M. SIMPSON, *J. Opt. Soc. Am. B* **2** (1985) 619.
35. G. ANGEL, R. GAGEL and A. LAUBEREAU, *Opt. Lett.* **14** (1989) 1005.
36. W. H. KNOX and F. A. BEISSER, *Opt. Lett.* **17** (1992) 1012.
37. F. SEIFERT and W. PETROV, *Opt. Commun.* **99** (1993) 413.
38. E. LILL, S. SCHNEIDER and F. DÖRR, *Opt. Commun.* **22** (1977) 107.
39. J. FURTHNER, H. SCHILLINGER and A. PENZKOFER, *Opt. Commun.* **78** (1990) 41.
40. D. R. DYKAAR and S. B. DARACK, *Opt. Lett.* **18** (1993) 634.
41. M. R. X. DE BARROS and P. C. BECKER, *Conference on Lasers and Electro-Optics, 1993*, Vol. 11, OSA Technical Digest Series (Optical Society of America, Washington, DC, 1993) p. 600.

42. J. M. EVANS, D. E. SPENCE, D. BURNS and W. SIBBETT, *Conference on Lasers and Electro-Optics, 1993*, Vol. 11, OSA Technical Digest Series (Optical Society of America, Washington, DC, 1993) p. 600.
43. W. KOECHNER, *Solid State Laser Engineering*, 3rd edn (Springer-Verlag, Heidelberg, 1992).
44. A. PENZKOFER and F. GRAF, *Opt. Quantum Electron.* **17** (1985) 252.
45. A. YARIV, *Optical Electronics*, 3rd edn (Holt, Rinehart and Winston, New York, 1985).
46. L. N. MAGDICH and V. Ya. MOLCHANOV, *Acousto-Optic Devices and Their Applications* (Gordon and Breach, New York, 1989).
47. A. PENZKOFER, *Appl. Phys. B* **46** (1988) 43.
48. H. VANHERZEELE, J. L. VAN ECK and A. E. SIEGMAN, *Appl. Opt.* **20** (1981) 3489.
49. D. R. PREUSS and J. L. GOLE, *Appl. Opt.* **19** (1980) 702.
50. J. FURTHNER and A. PENZKOFER, *Opt. Quantum Electron.* **24** (1992) 591.
51. F. GRAF and A. PENZKOFER, *Opt. Quantum Electron.* **17** (1985) 53.
52. A. SEILMEIER, B. KOPAINSKY and W. KAISER, *Appl. Phys.* **22** (1980) 355.
53. W. BLAU, W. DANKESREITER and A. PENZKOFER, *Chem. Phys.* **85** (1984) 473.
54. A. PENZKOFER and P. SPERBER, *Chem. Phys.* **88** (1984) 309.
55. H. SCHILLINGER and A. PENZKOFER, *Opt. Commun.* **68** (1988) 45.
56. Data sheet to Intra Action model ML-50Q acousto-optic modulator.
57. S. E. STOKOWSKI, R. A. SAROYAN and M. J. WEBER, *Nd-Doped Laser Glass Spectroscopic and Physical Properties* (Lawrence Livermore National Laboratory, University of California, Livermore, CA, 1981).
58. A. A. GRÜTTER, H. P. WEBER and R. DÄNDLIKER, *Phys. Rev.* **185** (1969) 629.
59. J. HERRMANN, F. WEIDNER and B. WILHELMI, *Appl. Phys. B* **26** (1981) 197.
60. M. HERCHER, *Appl. Opt.* **6** (1967) 947.
61. P. F. MOULTON, *J. Opt. Soc. Am. B* **3** (1986) 125.
62. J. M. EVANS, D. E. SPENCE, W. SIBBETT, B. H. T. CHAI and A. MILLER, *Opt. Lett.* **17** (1992) 1447.
63. A. MILLER, P. LI KAM WA, B. H. T. CHAI and E. W. VAN STRYLAND, *Opt. Lett.* **17** (1992) 195.
64. P. LI KAM WA, B. H. T. CHAI and A. MILLER, *Opt. Lett.* **17** (1992) 1438.
65. L. K. SMITH, S. A. PAYNE, W. L. KWAY, L. L. CHASE and B. H. T. CHAI, *IEEE J. Quantum Electron.* **QE-28** (1992) 2612.
66. A. SEAS, V. PETRIČEVIČ and R. R. ALFANO, *Opt. Lett.* **18** (1993) 891.
67. A. SENNAROGLU, C. R. POLLOCK and H. NATHEL, *Opt. Lett.* **18** (1993) 826.
68. T. V. HIGGINS, *Laser Focus World* **29/4** (1993) 133.
69. P. W. M. FRENCH, N. H. RIZVI, J. R. TAYLOR and A. V. SHESTAKOV, *Opt. Lett.* **18** (1993) 39.
70. Data sheet no. 2301, *Laser Glass* (Schott Glaswerke, Mainz, 1988).
71. D. VON DER LINDE and K. F. RODGERS, *IEEE J. Quantum Electron.* **QE-9** (1973) 960.